

1 **Growth of Clathrate Hydrates in Nanoscale Ice Films Observed**
2 **Using Electron Diffraction and Infrared Spectroscopy**

3 *Bijesh K. Malla¹, Ding-Shyue Yang^{2*}, and Thalappil Pradeep^{1,3*}*

4 ¹DST Unit of Nanoscience (DST UNS) and Thematic Unit of Excellence (TUE), Department of
5 Chemistry, Indian Institute of Technology Madras, Chennai 600036, India.

6 ² Department of Chemistry, University of Houston, Houston, Texas 77204, USA.

7 ³International Centre for Clean Water, IIT Madras Research Park, Chennai 600113, India.

8 **Corresponding authors**

9 ***Email:** yang@uh.edu, pradeep@iitm.ac.in

10 **Abstract**

11 Clathrate hydrates (CHs) are believed to exist in cold regions of space, such as comets and icy
12 moons. While spectroscopic studies have explored their formation in similar laboratory
13 conditions, direct structural characterization using diffraction techniques has remained elusive.
14 We present the first electron diffraction study of tetrahydrofuran (THF) and 1,3-dioxolane
15 (DIOX) CHs in the form of nanometer-thin ice films under ultrahigh vacuum at cryogenic
16 temperatures. By using reflection high-energy electron diffraction, we show that THF CH grows
17 readily on various substrates during thermal annealing of an amorphous ice mixture of THF and
18 water, and the formation is independent of the nature of the substrate. The growth of DIOX CHs
19 on an Au(111) substrate is similar. Comparison of electron diffraction patterns with calculated
20 XRD patterns indicates that THF and DIOX form structure II CH ($5^{12}6^4$) with a lattice constant
21 of ~ 17.2 Å (cubic, $Fd\bar{3}m$). Both CHs were also grown on Ru(0001) and were examined by
22 reflection absorption infrared spectroscopy. A direct comparison of diffraction data with infrared
23 spectra as a function of temperature further demonstrates the strength of multiple probes in
24 examining complex systems possessing diverse molecular interactions.

25 **Subjects**

26 Clathrate hydrates, Ultrahigh vacuum, Electron diffraction, Ice, Infrared spectroscopy

27 **Keywords**

28 Tetrahydrofuran, Dioxolane, RHEED, RAIRS, Cubic ice, Crystalline ice, Clathrates, Molecular
29 films

30 **Introduction**

31 Existence of Clathrate hydrates (CHs) in the simulated interstellar environment has been
32 established by infrared spectroscopy.¹ CHs represent a unique class of compounds where water
33 molecules form cages to encapsulate guest molecules, creating crystalline solids. This molecular
34 arrangement of water allows for the inclusion of a variety of molecules, such as CH₄, C₂H₆,
35 C₃H₈, CO₂, N₂, O₂, and others within the crystalline structures.² Typically, CHs exhibit three
36 crystalline structures: structure I (sI, cubic Pm $\bar{3}$ n), structure II (sII, cubic Fd $\bar{3}$ m), and structure H
37 (sH, hexagonal P6/mmm), and they generally occur under high-pressure conditions.³⁻⁵ Since the
38 detection of methane CH in 2019 at 30 K under ultrahigh vacuum (UHV) conditions⁶ principally
39 using reflection absorption infrared spectroscopy (RAIRS), there have been several reports on
40 the CHs of molecules. They include those of ethane (C₂H₆),⁷ formaldehyde (HCHO),⁸ acetone
41 (CH₃COH),⁹ acetaldehyde,¹⁰ tetrahydrofuran ((CH₂)₄O),^{11,12} and dimethyl ether (CH₃OCH₃).¹³
42 The formation of CHs occurs typically starting from an amorphous ice mixture of the guest and
43 host water molecules, upon slow thermal annealing. It was noted in the original report that
44 maintaining methane/water mixture at 30 K for 25 h produces a characteristic methane CH peak
45 at 3017 cm⁻¹, corresponding to the C-H stretch of CH₄ encaged in the 5¹² cage. Deconvolution of
46 this feature showed that 13% of total methane exists as CH under this condition. Since then, it
47 has been possible to encage different percentages of guest molecules in CHs under different
48 temperature conditions in UHV. CO₂, in particular, produces hydrate even at 10 K, for which the
49 infrared spectrum was known in the literature.^{14,15} Additionally, studies of interactions of low-
50 energy electrons and photons with various caged molecules have been conducted in UHV,
51 although these have not been explicitly assigned to CHs.¹⁶⁻¹⁸

52 A key question that comes up in such investigations is the independent confirmation of CHs
53 by structural tools, especially by using scattering techniques. As these experiments are conducted
54 on thin films with thicknesses in the nanometer (nm) scale, a suitable option for structural
55 characterization is electron diffraction.¹⁹⁻²¹ Electron diffraction in a transmission electron

56 spectroscope (of methanol CH) was reported in 1991, under 10^{-6} torr.¹⁴ However, no report exists
57 in UHV on any of the hydrates at temperatures below 160 K, which is typically the desorption
58 temperature of water in UHV conditions.²² Considering the nature of RAIRS conducted on
59 single-crystal surfaces, a natural choice for structural studies is reflection high energy electron
60 diffraction (RHEED). It is a well-suited technique for studying the structures and phase
61 transitions of solid-supported molecular thin films, and our lab has conducted several
62 experiments in this regard.²³⁻²⁸ In the present work, we report the first RHEED experiment of
63 tetrahydrofuran (THF-C₄H₈O) and 1,3-dioxolane (DIOX-C₃H₆O₂) CHs under UHV, and the
64 results were compared with simulated diffraction data. The emergence of CHs under the same
65 temperature and pressure conditions was confirmed by RAIRS. Although THF and DIOX have
66 not yet been detected in the ISM, various similar molecules, such as dimethyl ether, propylene
67 oxide, and ethylene oxide, have been identified.²⁹⁻³¹ Given the ongoing advancements in
68 astronomical observations, the detection of THF and DIOX in the ISM may be possible in near
69 future. We believe that these investigations further enrich our understanding of the formation of
70 CHs in UHV and cryogenic conditions and present opportunities for their exploration using other
71 UHV techniques, such as low-energy ion scattering.^{32,33} It is worth noting that while the RHEED
72 and RAIRS measurements were performed on separate instruments, both were conducted under
73 identical temperature and pressure conditions to ensure consistency. For the RHEED
74 experiments, ice films were grown on three distinct substrates: highly oriented pyrolytic graphite
75 (HOPG, ZYA grade), single-crystalline Au(111) (Princeton Scientific), and a hydrophobic self-
76 assembled monolayer (SAM) of 1-octadecanethiol on Au(111). Co-deposition methods were
77 employed to create thin films of ice with an approximate thickness of 25 nm for CH preparation.
78 This process involved the simultaneous deposition of pre-mixed vapors of THF or DIOX with
79 water for 10 min. For the RAIRS experiments, the Ru(0001) substrate was used to prepare thin
80 ice films. A mixed ice film with an approximate thickness of 60 nm, composed of THF/DIOX
81 and water in a 1:3 ratio, was prepared on the Ru(0001) substrate at 105 K. This was achieved by
82 backfilling the chamber with THF/DIOX and water vapor for a duration of 10 minutes at a total
83 pressure of 5×10^{-7} mbar. The experimental procedures and ice thickness calculations for both
84 RHEED and RAIRS are detailed in the Supporting Information. Calculated X-ray diffraction
85 (XRD) patterns are shown in Figure 1b, d for cubic ice (ice Ic) ($a = 6.35 \text{ \AA}^{-1}$)³⁴ and THF CH ($a =$
86 17.21 \AA^{-1})³⁵ along with Figure S4 for hexagonal ice (ice Ih) ($a/b = 4.49 \text{ \AA}^{-1}$, $c = 7.33 \text{ \AA}^{-1}$)³⁶

were calculated using the VESTA software.³⁷ These patterns were compared with the experimental electron diffraction patterns to validate the phase identification.

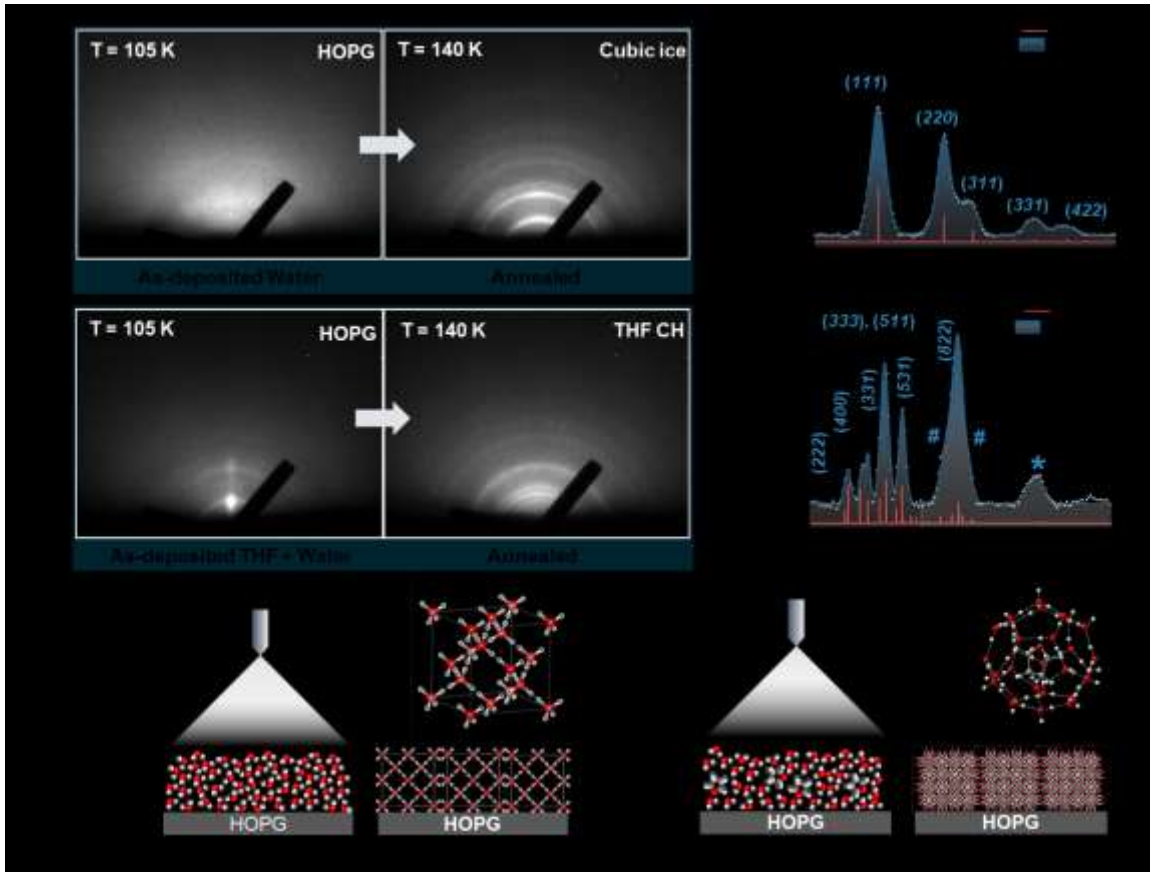


Figure 1. Evolution of ice Ic and THF CH explored with RHEED. (a) Electron diffraction images of as-deposited water on HOPG at 105 K and after annealing to 140 K. (b) Comparison of the experimental radially-averaged electron diffractions of annealed water ice at 140 K with the calculated diffraction peaks (red lines) of ice Ic. (c) Electron diffraction images of as-deposited THF-water ice mixture on HOPG at 105 K and after annealing to 140 K. (d) Comparison of the experimental radially-averaged electron diffractions of annealed THF-water ice at 140 K with the calculated (red lines) diffraction peaks of sII THF CH. Peaks labeled with # are attributed to ice Ic, while that marked with * corresponds to the collection of low-intensity signals of THF CH, shown in the theoretical spectrum. (e) Schematic diagram of the formation of ice Ic on HOPG from vapor-deposited ice. (f) Schematic diagram of the formation of sII THF-CH on HOPG from vapor-deposited ice.

89 In Figure 1, we present the evolution of ice Ic and CH of THF grown on HOPG in the
90 temperature window of 105 to 140 K. Under high vacuum ($\sim 10^{-6}$ - 10^{-8} mbar) conditions,
91 amorphous ice typically crystallizes into ice Ic, ice Ih, or stacking-disordered ice.³⁸⁻⁴¹ The crystal
92 structure may be significantly influenced by the substrate and the temperature.²⁰ Prior to
93 investigating the formation of CH, we commenced our study with an examination of the
94 structure of pure ice, as these are well-characterized by RHEED.^{21,23} Figure 1a shows the
95 RHEED images of as-deposited water ice on HOPG and after its annealing to 140 K. Amorphous
96 solid water (ASW) of approximately 120 nm thickness was accumulated on the HOPG surface
97 by vapor deposition of water in UHV conditions as shown in Figure 1e. Diffuse scattering with
98 broad ring-like features at 105 K (Figure 1a) indicates low-density ASW with only a short-range
99 order for the as-deposited ice. After annealing to 140 K, sharper Debye–Scherrer rings emerge in
100 the electron diffraction pattern, which indicates the crystallization of ASW into a randomly
101 oriented polycrystalline specimen around 140 K (Figure 1a). This ring pattern is unchanged till
102 the desorption of ice. Figure 1b presents a comparison between the experimental radially-
103 averaged electron diffraction intensity curves as a function of momentum transfer, $s = (4\pi/\lambda)$
104 $\sin(\theta/2)$, where θ is the total angle of scattering and the calculated X-ray diffraction spectrum for
105 ice Ic. The observed positions of the (111), (220), (311), (331), and (442) electron diffraction
106 peaks of ice Ic match well with the calculated values, indicating the formation of ice Ic with a
107 lattice constant of $a = 6.35$ Å.^{23,34,42} The large diffraction width is the result of a finite crystallite
108 size of a few nm on average, estimated according to the Scherrer formula.²³

109 To create THF CH, THF-water mixed vapor was co-deposited on HOPG substrate at 105 K
110 and then annealed to higher temperatures (Figure 1, c and f). At 105 K (Figure 1c), the
111 observation of electron diffraction spots and diffuse ring patterns suggests the formation of
112 crystalline THF in ASW. This may be understood because vapor deposition of pure THF on
113 HOPG at 105 K results in a RHEED pattern of clear electron diffraction spots without rings,
114 which signifies an ordered crystalline phase with respect to the supporting surface (Figure S1).
115 Additionally, RAIRS study showed that THF undergoes a phase transition from an amorphous
116 assembly to a crystalline phase near 90 K (Figure S2). Upon thermal annealing the ice mixture to
117 140 K, the initial electron diffraction spots disappear, and new Debye–Scherrer rings emerge,
118 which are substantially different from those of ice Ic (Figure 1, b, and d). Concurrently, during
119 the thermal annealing process, an increase in the chamber pressure was noted, indicating the

120 partial desorption of THF from the water ice matrix as evidenced by the gradual disappearance of
121 the electron diffraction spots (Figure S3). The loss of THF from the ice matrix during annealing
122 was again confirmed by the RAIRS study (Figure 4). This desorption as a result of increased
123 mobility, likely facilitates intermolecular motions of THF, leading to the formation of THF-CH.

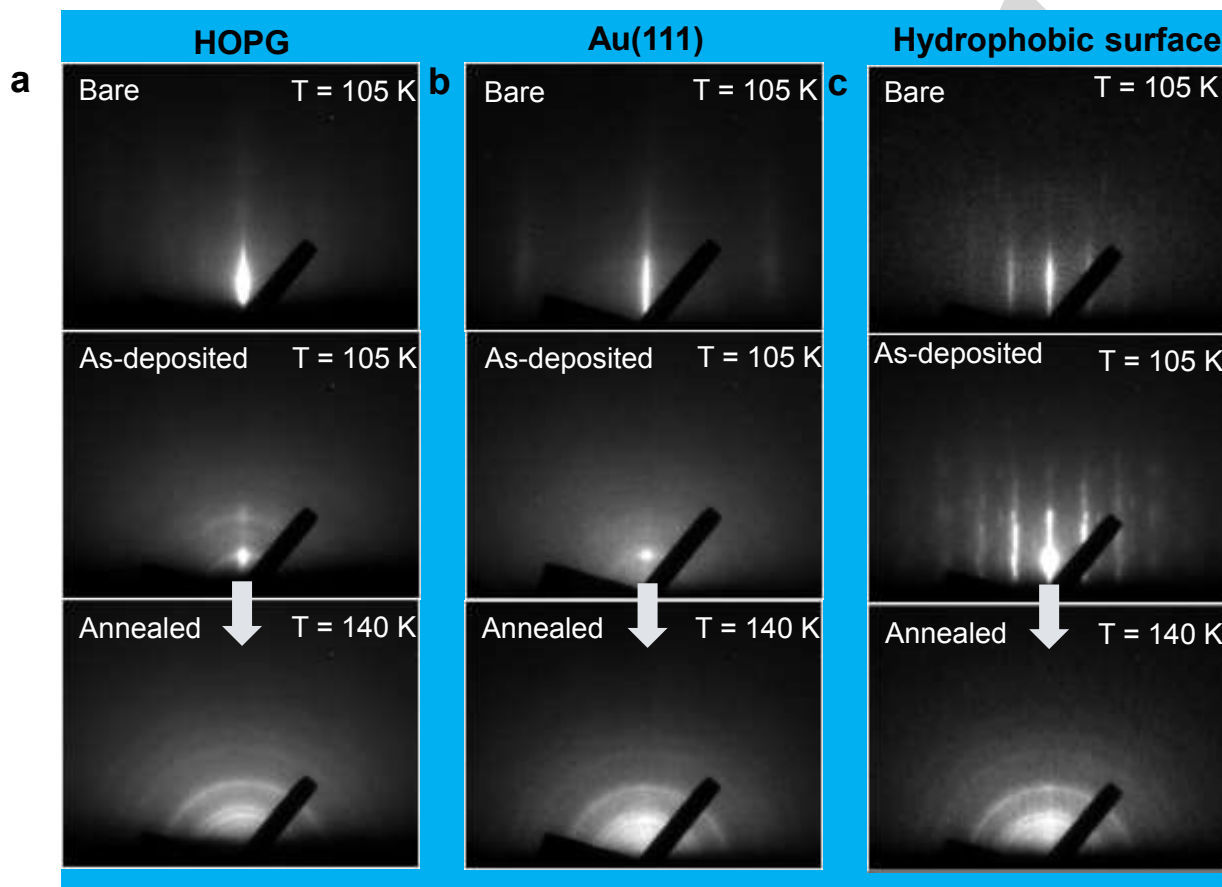


Figure 2. Evolution of THF-CH on HOPG, Au(111), and hydrophobic surface (SAM of 1-octadecanethiol on Au(111)). The RHEED images, displayed vertically, show bare HOPG (a), Au(111) (b), and a hydrophobic surface (c) at 105 K (top row), as-deposited THF-water ice mixture on the respective substrate at 105 K (middle row), and the same ice mixture on the respective substrate after annealing at 140 K (bottom row).

124

125 Radially averaged electron diffraction intensities were calculated from the RHEED image of
 126 Figure 1b at 140 K and were compared with the calculated diffraction peaks for sII THF CH.³¹
 127 Agreement of the positions of high-intensity peaks is satisfactory, which signifies the presence of
 128 sII THF CH with a cubic lattice of $a = 17.2 \text{ \AA}$.^{35,43} The relatively smaller peaks corresponding to
 129 the (220) and (331) diffractions of ice Ic were noted (marked by # in Figure 1d), suggesting a
 130 minor fraction of ice Ic within the thin film. For clarity, a comparison of the observed and

Table 1. Electron diffraction results for ice Ic, sII THF, and DIOX CH. Calculated and observed hkl (crystallographic indices), and d (Bragg distance).

Cubic ice Cal.		Cubic ice Obs.		sII THF CH Cal.		sII THF CH Obs.		sII DIOX CH Obs.	
hkl	d	hkl	d	hkl	d	hkl	d	hkl	d
				111(s)	9.94				
				311(w)	5.19	5.10 ^s			
				222(s)	4.97	4.98 ^{&}			
				400(s)	4.30	4.31 ^s			
				331(s)	3.94	3.93 ^s	3.92		
111(s)	3.67(s)	3.68		422(s)	3.51	3.50 ^s			
				333/511(s)	3.31	3.30 ^{&}	3.33 ^{&}		
				440 (w)	3.04				
				531(s)	2.91	2.90	2.94		
				620 (w)	2.72				
				533(w)	2.62				
220(s)	2.24(s)	2.24		731(w)	2.24	2.21 ^s	2.21 ^s		
				733(w)	2.10	2.02 ^s			
				822/660(s)	2.02	2.03 ^{&}	2.03 ^{&}		
				555/751(w)	1.98				
311(s)	1.91(s)	1.96				1.92 ^s	1.92 ^s		
331(s)	1.45(s)	1.47							
422(s)	1.29(s)	1.29							

Calculated d -values (in \AA^{-1}) are obtained using $a = 6.35 \text{ \AA}^{-1}$ for ice Ic and 17.21 \AA^{-1} for THF CH. The symbols & and \$ represent the composite broad peak having a peak center at the d value shown and the peak that combines with a broad peak, s represents strong peak intensity, and w represents weak peak intensity.

131 calculated interplanar distances of ice Ic and THF CH is provided in Table 1. The possible
132 presence of ice Ih contributing to stacking disorder was also considered, and a comparison of the
133 calculated diffraction patterns of ice Ic, ice Ih, and THF CH against the experimental electron
134 diffraction of THF CH is provided in Figure S4. Although stacking faults are present, their
135 occurrence is expected to be very minimal in polycrystalline ice.

136 The formation of ice Ic and ice Ih significantly depends on the substrate structure, as shown
137 in the literature^{19,20}, but the emergence of clathrate hydrate is independent of the substrates used
138 for deposition. This was established by conducting the same experiments on two other substrates:
139 Au(111) and self-assembled monolayer (SAM) of 1-octadecanethiol on Au(111), a hydrophobic
140 surface. The electron diffraction streaks seen in the top row of Figure 2 correspond to the ordered
141 structures of the bare surfaces.⁴⁴ Evidently, the same ring pattern was obtained at 140 K (Figure
142 2, bottom row), indicating CH formation on these substrates even though the initial thin-film
143 structures may exhibit differences (Figure 2, middle row). This confirmed that regardless of the
144 interface, THF and water formed CH around 140 K.

145 To examine the preference of CH formation in UHV conditions, we conducted experiments
146 with 1,3-dioxolane (DIOX), another guest for stable CHs. To create DIOX CH, mixed vapor of
147 DIOX-water was deposited on Au(111) substrate at 105 K and annealed to 140 K. At 105 K, the
148 diffused RHEED pattern seen from the as-deposited mixture of DIOX and water molecules
149 indicates the largely amorphous nature of the ice mixture. The electron diffraction spots suggest
150 the formation of DIOX crystallites, as noted in Figure 1c. After annealing to 140 K, the same
151 Debye–Scherrer rings appeared as in the case of THF CH (Figure 3a). The experimental and
152 calculated Bragg diffractions and their corresponding interplanar distances are compared in Table
153 1. Here, it is worth noting that the experimentally obtained electron diffraction pattern of DIOX
154 CH is compared with the calculated XRD pattern of THF CH due to the unavailability of the
155 crystallographic information file (CIF) for DIOX CH. DIOX is known to form sII CH under
156 high-pressure conditions and has a lattice constant similar to that of THF,⁴³ with comparable van
157 der Waals radii (THF: 2.95 Å; DIOX: 2.8 Å).⁴⁵ XRD patterns of CHs formed by different
158 molecules are comparable if they adopt the same hydrate structure.³ This comparability has been
159 utilized in selected area electron diffraction studies of methanol CH, with ethanol and THF, as
160 they all form sII CH.¹⁴ In our study, we note that the positions of the (331), (333)/(511), (531),

161 and (822) electron diffractions match well with the calculated peaks of sII THF CH. Additionally,
 162 the formation of a minor fraction of ice Ic was confirmed by the presence of the (220) and (331)
 163 intensities (Figure 3b). These electron diffraction results confirm the successful formation of sII
 164 CH of DIOX at 140 K in UHV.

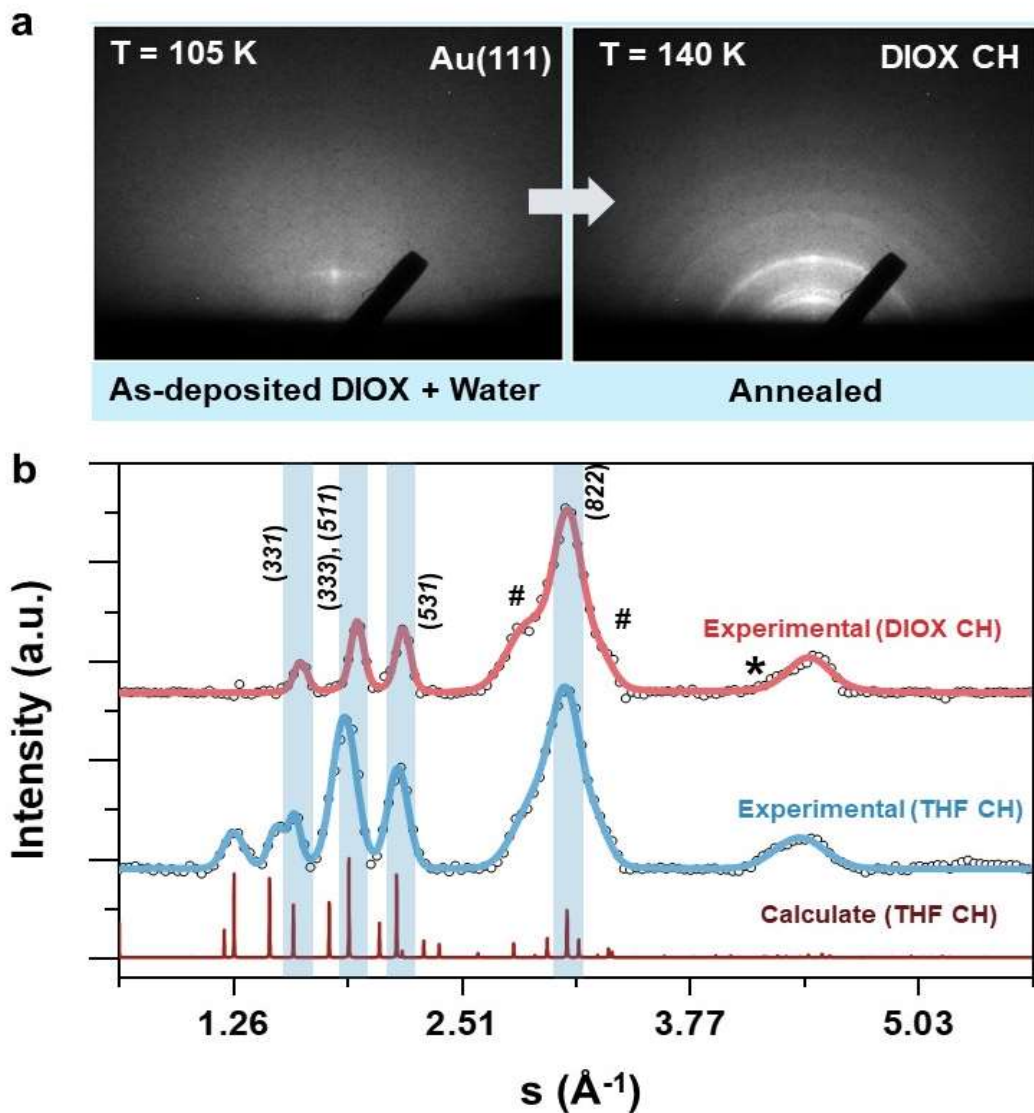


Figure 3. CH formation of DIOX studied using RHEED. (a) Diffraction images of as-deposited water on DIOX substrate at 105 K and after annealing to 140 K. (b) The experimental radially averaged diffraction pattern of annealed DIOX-water ice and that of the annealed THF-water ice, both at 140 K, compared with the calculated diffraction pattern of sII THF-CH. Peaks labeled with # are attributed to ice Ic, while that marked with * corresponds to the collection of low-intensity signals of DIOX CH, shown in theoretical THF CH.

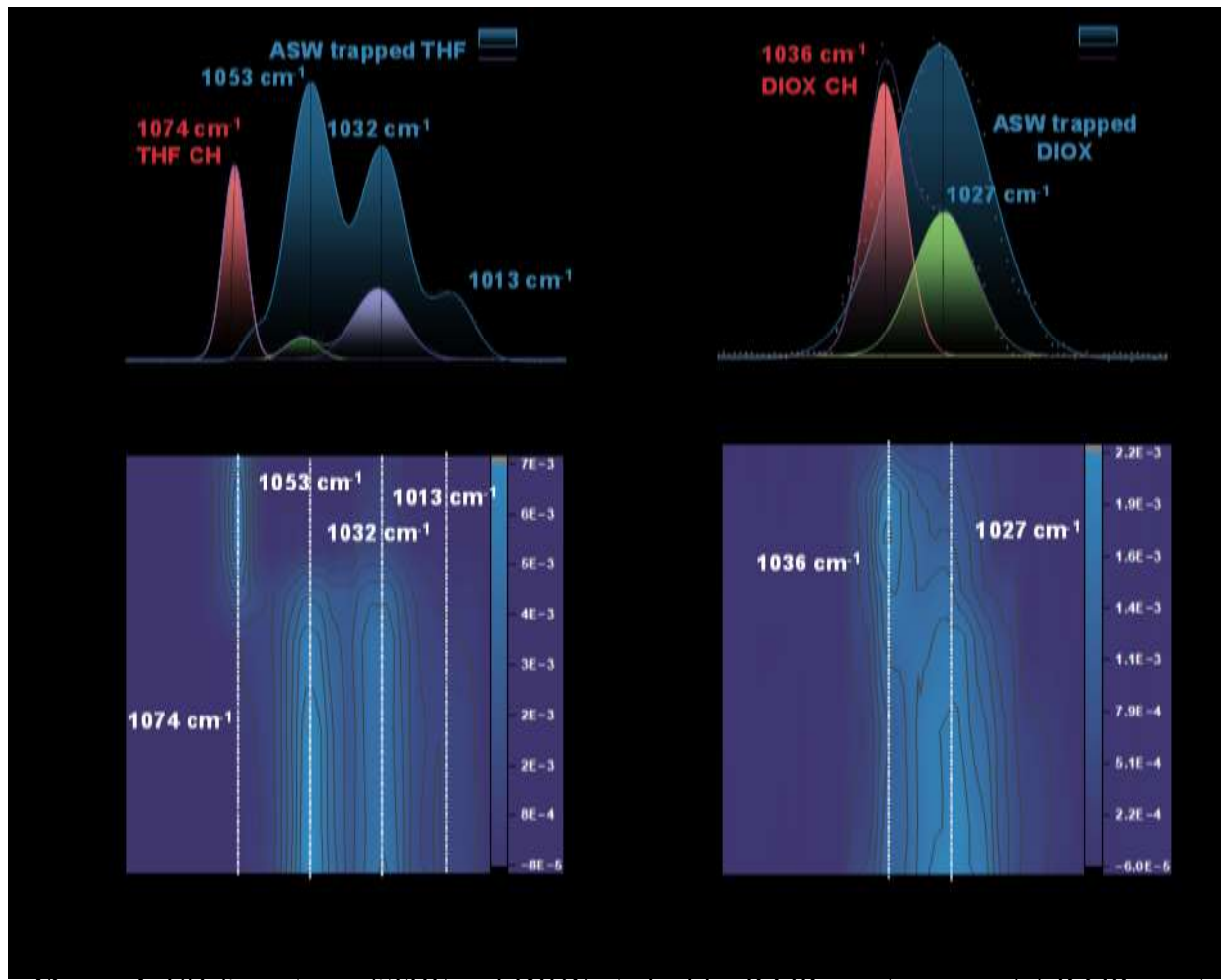


Figure 4. CH formation of THF and DIOX studied by RAIR spectroscopy. (a) RAIR spectra of THF-water ice mixture in the C-O antisymmetric stretching region of THF at 105 K and 140 K, respectively. At 140 K, RAIR spectrum is deconvoluted into three components, highlighted in red (1074 cm^{-1}), green (1053 cm^{-1}), and violet (1032 cm^{-1}) colors (b) RAIR spectra of DIOX-water ice mixture in C-O ring stretching region of DIOX at 105 K and 140 K, respectively. At 140 K RAIR spectrum is deconvoluted into two components, highlighted in red (1036 cm^{-1}) and green (1027 cm^{-1}) colors. Temperature-dependent evolution of different peaks in the C-O antisymmetric stretching region of THF (c) in THF-water ice mixture and C-O ring stretch stretching region of DIOX (d) in DIOX-water ice mixture.

165 The formation of CHs of THF and DIOX was further investigated using RAIRS. To form the
 166 CH, vapors of THF and water were co-deposited on a Ru(0001) substrate at 105 K and annealed
 167 to 140 K with a ramping rate of 2 K/min. Figure 4a shows the RAIR spectra of THF-water ice
 168 mixture at 105 K and 140 K in the C-O antisymmetric stretching region of THF. RAIR spectrum

169 at 105 K shows three peaks at 1053, 1032, and 1013 cm^{-1} and a weak broad peak around 1069
170 cm^{-1} , which are attributed to different fractions of THF trapped in ASW, with different hydrogen
171 bonding structures of the ice matrix. After annealing to 140 K, a new peak emerges at 1074 cm^{-1} ,
172 which is attributed to THF trapped in the large cage ($5^{12}6^4$) of sII CH. From the RAIR spectrum,
173 it is evident that there are some uncaged THF remaining in the matrix at 140 K. The decrease in
174 the band area of RAIR spectra after annealing indicates the loss of THF due to its desorption.
175 Analysis of the band areas revealed that only 17.4% of the total deposited THF forms CH, while
176 16.5% remains uncaged in the ice matrix, and 66.1% desorbs. In Figure 4c, the temperature-
177 dependent evolution of THF CH is shown. THF CH formation started around 130 K, and the
178 fraction kept on increasing till 150 K.

179 For the formation of DIOX CH, DIOX and water vapors were co-deposited on Ru(0001)
180 substrate at 105 K and annealed to 140 K. Figure 4b shows the RAIR spectra of DIOX-water ice
181 mixture at 105 K and 140 K in the C-O ring stretching region. At 105 K, the peak at 1027 cm^{-1}
182 indicates amorphous DIOX, trapped in ASW; the same peak was compared with pure amorphous
183 DIOX (Figure S5). Upon annealing to 140 K, a new peak emerged at 1036 cm^{-1} (Figure 4b),
184 indicating the formation of DIOX CH, where DIOX molecules were trapped in the $5^{12}6^4$ cages of
185 the sII hydrate structure. Simultaneously, there was a notable decrease in the peak intensity at
186 1027 cm^{-1} , corresponding to the trapped DIOX in the ice matrix. The observed blue shift in the
187 peak position is attributed to the interaction between DIOX molecules and the host hydrate
188 cages, reflecting a change in the molecular environment. Deconvolution of the RAIR spectrum at
189 140 K revealed that 35% of DIOX forms CH, while 28% remains uncaged within the ice matrix
190 from the total deposited DIOX molecules. In Figure 4d, the temperature-dependent evolution of
191 DIOX CH is shown, where DIOX CH started growing at 130 K. The electron diffraction data
192 (Figure 1 and Figure 3) showed the formation of sII CH of THF and DIOX. The IR results
193 provide evidence for the formation of $5^{12}6^4$ cages of sII. We note that while RHEED provides
194 structural details of the topmost monolayers, RAIRS offers information about the entire thin film
195 of ice. From the above results, it is evident that CH formation is facile in a nm-thin amorphous
196 ice mixture in UHV conditions at a suitable temperature where the intermolecular mobility is
197 high. Formation of CHs on different substrates proved that the structure of the interface does not
198 significantly affect the nucleation of CHs.

199 The nucleation of CHs in amorphous solids can be classified as homogeneous nucleation due
200 to the absence of any observable surface effects.⁵ Under high-pressure conditions, two
201 intermediate pathways are predicted for CH nucleation, theoretically.⁴⁶ One pathway follows the
202 crystalline critical nucleus, while the other involves an amorphous critical nucleus as an
203 intermediate step before transitioning into crystalline CH. Specifically, in the case of amorphous
204 critical nucleation, a metastable amorphous CH is initially formed, which requires an additional
205 activation barrier to convert into its crystalline form.^{5,46-48} In our system, starting with an
206 amorphous mixture of water and guest molecules, the formation of a critical amorphous nucleus
207 may be favored, which, upon increasing the temperature, results in the crystallization of CHs.
208 Our previous study demonstrated that at 120 K, the majority of THF forms CHs after a 110 h
209 incubation period, which is significantly reduced to 6 h at 135 K; however, the current RHEED
210 results indicate that at 140 K, CH formation occurs rapidly, with minimal time required for
211 nucleation. The activation energy for this process was found to be 23.12 kJ mol⁻¹, lower than that
212 required for the crystallization of ASW.⁸ Based on these findings, we propose that CH formation
213 under ultra-high vacuum conditions likely follows the amorphous critical nucleation pathway. In
214 this scenario, some molecules forming metastable amorphous CHs may fail to crystallize and
215 will subsequently decompose into either ice Ic or ice Ih.^{9,10,13} To validate this suggestion,
216 nucleation at the molecular level may be examined using cryo-electron microscopy and we will
217 be pursuing this in future.

218 The data presented in this study confirmed the formation of CHs in ultrahigh vacuum
219 conditions under cryogenic temperatures, as evidenced by RAIRS and RHEED data. Both THF
220 and DIOX demonstrated the formation of CHs upon gradual thermal annealing around 140 K,
221 where intermolecular motion of water becomes possible. The RHEED data were compared with
222 the available XRD data. This CH formation was shown to be substrate-independent, as similar
223 results were obtained on HOPG, Au(111), and a hydrophobic self-assembled monolayer
224 substrate. While this study specifically focuses on two guest molecules, a direct comparison of
225 electron diffraction data with infrared spectra of several CHs would expand the scope of this
226 research, facilitating the study of diverse molecular interactions in cryogenic conditions. The
227 confirmation of CH formation by electron diffraction and spectroscopy on different substrates
228 may offer additional support for their existence in space.

229 **ASSOCIATED CONTENT**

230 Supporting Information is available free of charge. It includes Experimental Section, RHEED
231 images of pure THF, electron diffraction spectra, and RAIRS of pure THF and DIOX.

232 **AUTHOR INFORMATION**

233 **Corresponding authors**

234 **Thalappil Pradeep** - *Department of Science and Technology Unit of Nanoscience (DST UNS)*
235 *and Thematic Unit of Excellence (TUE), Department of Chemistry, Indian Institute of*
236 *Technology Madras, Chennai 600036, India, International Centre for Clean Water, IIT Madras*
237 *Research Park, Chennai 600113, India, and Centre of Excellence on Molecular Materials and*
238 *Functions, Indian Institute of Technology Madras, Chennai 600036, India*

239 Email: pradeep@iitm.ac.in

240 **Ding-Shyue Yang** - *Department of Chemistry, University of Houston, Houston, Texas 77204,*
241 *USA.*

242 Email: yang@uh.edu

243 **Authors**

244 **Bijesh K. Malla** -*Department of Science and Technology Unit of Nanoscience (DST UNS) and*
245 *Thematic Unit of Excellence (TUE), Department of Chemistry, Indian Institute of Technology*
246 *Madras, Chennai 600036, India*

247 **Authors Contributions**

248 T.P., D.-S.Y., and B.K.M. designed the research. D.-S.Y. and B.K.M. have performed the
249 experiments and analyzed the results. T.P. and D.-S.Y supervised its progress. The manuscript
250 was prepared with contributions from all authors.

251 **Notes**

252 The authors declare no competing financial interests.

253 **ACKNOWLEDGMENT**

254 We acknowledge the Science and Engineering Research Board (SERB), Department of Science
255 and Technology (DST), and Government of India for research funding. T.P. acknowledges
256 funding from the Centre of Excellence on Molecular Materials and Functions under the
257 Institution of Eminence scheme of IIT Madras. D.-S.Y. acknowledges the support of the National

258 Science Foundation (CHE-2154363). B.K.M. thanks the Council of Scientific and Industrial
259 Research (CSIR) for his research fellowship. B.K.M. was a recipient of the International
260 Immersion Experience (IIE) travel fellowship of IIT Madras.

261 **REFERENCES**

262 (1) Ghosh, J.; Vishwakarma, G.; Kumar, R.; Pradeep, T. Formation and Transformation of
263 Clathrate Hydrates under Interstellar Conditions. *Acc. Chem. Res.* **2023**, *56* (16), 2241–
264 2252.

265 (2) Sloan, E. D. J.; Koh, C. A. Introduction: Clathrate Hydrates of Natural Gases. *Clathrate*
266 *Hydrates Nat. Gases* **2008**, I–XXV.

267 (3) Sloan Jr., E. D.; Koh, C. A.; Koh, C. A. *Clathrate Hydrates of Natural Gases*; CRC Press,
268 2007.

269 (4) Chong, Z. R.; Yang, S. H. B.; Babu, P.; Linga, P.; Li, X.-S. Review of Natural Gas
270 Hydrates as an Energy Resource: Prospects and Challenges. *Appl. Energy* **2016**, *162*,
271 1633–1652.

272 (5) Khurana, M.; Yin, Z.; Linga, P. A Review of Clathrate Hydrate Nucleation. *ACS Sustain.*
273 *Chem. Eng.* **2017**, *5* (12), 11176–11203.

274 (6) Ghosh, J.; Methikkalam, R. R. J.; Bhuin, R. G.; Ragupathy, G.; Choudhary, N.; Kumar,
275 R.; Pradeep, T. Clathrate Hydrates in Interstellar Environment. *Proc. Natl. Acad. Sci. U. S.*
276 *A.* **2019**, *116* (5), 1526–1531.

277 (7) Malla, B. K.; Vishwakarma, G.; Chowdhury, S.; Selvarajan, P.; Pradeep, T. Formation of
278 Ethane Clathrate Hydrate in Ultrahigh Vacuum by Thermal Annealing. *J. Phys. Chem. C*
279 **2022**, *126* (42), 17983–17989.

280 (8) Ghosh, J.; Vishwakarma, G.; Das, S.; Pradeep, T. Facile Crystallization of Ice Ih via
281 Formaldehyde Hydrate in Ultrahigh Vacuum under Cryogenic Conditions. *J. Phys. Chem. C*
282 **2021**, *125* (8), 4532–4539.

283 (9) Ghosh, J.; Bhuin, R. G.; Vishwakarma, G.; Pradeep, T. Formation of Cubic Ice via
284 Clathrate Hydrate, Prepared in Ultrahigh Vacuum under Cryogenic Conditions. *J. Phys.*
285 *Chem. Lett.* **2020**, *11* (1), 26–32.

286 (10) Vishwakarma, G.; Malla, B. K.; Chowdhury, S.; Khandare, S. P.; Pradeep, T. Existence of
287 Acetaldehyde Clathrate Hydrate and Its Dissociation Leading to Cubic Ice under
288 Ultrahigh Vacuum and Cryogenic Conditions. *J. Phys. Chem. Lett.* **2023**, *14*, 5328–5334.

289 (11) Ghosh, J.; Bhuin, R. G.; Ragupathy, G.; Pradeep, T. Spontaneous Formation of
290 Tetrahydrofuran Hydrate in Ultrahigh Vacuum. *J. Phys. Chem. C* **2019**, *123* (26), 16300–
291 16307.

292 (12) Vishwakarma, G.; Malla, B. K.; Reddy, K. S. S. V. P.; Ghosh, J.; Chowdhury, S.;
293 Yamijala, S. S. R. K. C.; Reddy, S. K.; Kumar, R.; Pradeep, T. Induced Migration of CO₂
294 from Hydrate Cages to Amorphous Solid Water under Ultrahigh Vacuum and Cryogenic
295 Conditions. *J. Phys. Chem. Lett.* **2023**, *14*, 2823–2829.

296 (13) Malla, B. K.; Vishwakarma, G.; Chowdhury, S.; Nayak, S. K.; Yamijala, S. S. R. K. C.;
297 Pradeep, T. Formation and Dissociation of Dimethyl Ether Clathrate Hydrate in
298 Interstellar Ice Mimics. *J. Phys. Chem. C* **2024**, *128* (6), 2463–2470.

299 (14) Blake, D.; Allamandola, L.; Sandford, S.; Hudgins, D.; Freund, F. Clathrate Hydrate
300 Formation in Amorphous Cometary Ice Analogs in Vacuo. *Science*. **1991**, *254* (5031),
301 548–551.

302 (15) Fleyfel, F.; Devlin, J. P. Carbon Dioxide Clathrate Hydrate Epitaxial Growth:
303 Spectroscopic Evidence for Formation of the Simple Type-II CO₂ Hydrate. *J. Phys.*
304 *Chem.* **1991**, *95* (9), 3811–3815.

305 (16) Ramakrishnan, S.; Sagi, R.; Mahapatra, N.; Asscher, M. Effect of Coadsorbed Oxygen on
306 the Photochemistry of Methane Embedded in Amorphous Solid Water. *J. Phys. Chem. C*
307 **2018**, *122* (27), 15287–15296.

308 (17) Ayoub, Y.; Asscher, M. Interaction of Ethyl Chloride with Amorphous Solid Water Thin
309 Film on Ru(001) and O/Ru(001) Surfaces. *J. Phys. Chem. A* **2009**, *113* (26), 7514–7520.

310 (18) Horowitz, Y.; Asscher, M. Electron-Induced Chemistry of Methyl Chloride Caged within
311 Amorphous Solid Water. *J. Chem. Phys.* **2013**, *139* (15), 154707.

312 (19) Souda, R.; Aizawa, T. Reflection High Energy Electron Diffraction (RHEED) Study of
313 Ice Nucleation and Growth on Ni(111): Influences of Adspecies and Electron Irradiation.
314 *Phys. Chem. Chem. Phys.* **2019**, *21* (35), 19585–19593.

315 (20) Souda, R.; Aizawa, T.; Sugiyama, N.; Takeguchi, M. Structure Analysis of Water Ice
316 Crystallites on NaCl(001), KCl(001), and CaF₂(111) by Reflection High-Energy Electron
317 Diffraction. *J. Phys. Chem. C* **2020**, *124* (28), 15180–15187.

318 (21) Yang, D. S.; Zewail, A. H. Ordered Water Structure at Hydrophobic Graphite Interfaces
319 Observed by 4D, Ultrafast Electron Crystallography. *Proc. Natl. Acad. Sci.* **2009**, *106*

320 (11), 4122–4126.

321 (22) Minissale, M.; Aikawa, Y.; Bergin, E.; Bertin, M.; Brown, W. A.; Cazaux, S.; Charnley,
322 S. B.; Coutens, A.; Cuppen, H. M.; Guzman, V.; et al. Thermal Desorption of Interstellar
323 Ices: A Review on the Controlling Parameters and Their Implications from Snowlines to
324 Chemical Complexity. *ACS Earth Sp. Chem.* **2022**, *6* (3), 597–630.

325 (23) Yang, D.-S.; He, X. Structures and Ultrafast Dynamics of Interfacial Water Assemblies on
326 Smooth Hydrophobic Surfaces. *Chem. Phys. Lett.* **2017**, *683*, 625–632.

327 (24) He, X.; Wu, C.; Rajagopal, K.; Punpongjareorn, N.; Yang, D. S. Ordered Ionic Liquid
328 Structure Observed at Terraced Graphite Interfaces. *Phys. Chem. Chem. Phys.* **2016**, *18*
329 (5), 3392–3396.

330 (25) Wu, C.; Yang, D. S. Ordered Structures and Morphology-Induced Phase Transitions at
331 Graphite-Acetonitrile Interfaces. *J. Phys. Chem. C* **2019**, *123* (36), 22390–22396.

332 (26) He, X.; Wu, C.; Yang, D.-S. Communication: No Guidance Needed: Ordered Structures
333 and Transformations of Thin Methanol Ice on Hydrophobic Surfaces. *J. Chem. Phys.*
334 **2016**, *145* (17).

335 (27) He, X.; Yang, D. S. Order-Determined Structural and Energy Transport Dynamics in
336 Solid-Supported Interfacial Methanol. *Nano Lett.* **2021**, *21* (3), 1440–1445.

337 (28) He, X.; Yang, D. S. Ethanol on Graphite: Ordered Structures and Delicate Balance of
338 Interfacial and Intermolecular Forces. *J. Phys. Chem. C* **2021**, *125* (43), 24145–24154.

339 (29) Snyder, L. E.; Buhl, D.; Schwartz, P. R.; Clark, F. O.; Johnson, D. R.; Lovas, F. J.;
340 Giguere, P. T. Radio Detection of Interstellar Dimethyl Ether. *Astrophys. J.* **1974**, *191*,
341 L79.

342 (30) McGuire, B. A.; Carroll, P. B.; Loomis, R. A.; Finneran, I. A.; Jewell, P. R.; Remijan, A.
343 J.; Blake, G. A. Detection of Interstellar Ethylene Oxide (c-C₂H₄O). *Science*. **2016**, *352*
344 (6292), 1449–1452.

345 (31) McGuire, B. A.; Carroll, P. B.; Loomis, R. A.; Finneran, I. A.; Jewell, P. R.; Remijan, A.
346 J.; Blake, G. A. Discovery of the Interstellar Chiral Molecule Propylene Oxide
347 (CH₃CHCH₂O). *Science*. **2016**, *352* (6292), 1449–1452.

348 (32) Cyriac, J.; Pradeep, T.; Kang, H.; Souda, R.; Cooks, R. G. Low-Energy Ionic Collisions at
349 Molecular Solids. *Chem. Rev.* **2012**, *112* (10), 5356–5411.

350 (33) Kang, H. Chemistry of Ice Surfaces. Elementary Reaction Steps on Ice Studied by

351 Reactive Ion Scattering. *Acc. Chem. Res.* **2005**, *38* (12), 893–900.
352 <https://doi.org/10.1021/AR0501471>.

353 (34) Jenniskens, P.; Blake, D. F. Structural Transitions in Amorphous Water Ice and
354 Astrophysical Implications. *Science*. **1994**, *265* (5173), 753–756.

355 (35) Dobrzycki, L.; Taraszewska, P.; Boese, R.; Cyrański, M. K. Pyrrolidine and Its Hydrates
356 in the Solid State. *Cryst. Growth Des.* **2015**, *15* (10), 4804–4812.

357 (36) Dowell, L. G.; Rinfret, A. P. Low-Temperature Forms of Ice as Studied by X-Ray
358 Diffraction. *Nat.* **1960**, *188* (4757), 1144–1148.

359 (37) Momma, K.; Izumi, F. VESTA 3 for Three-Dimensional Visualization of Crystal,
360 Volumetric and Morphology Data. *J. Appl. Crystallogr.* **2011**, *44* (6), 1272–1276.

361 (38) Huang, X.; Wang, L.; Liu, K.; Liao, L.; Sun, H.; Wang, J.; Tian, X.; Xu, Z.; Wang, W.;
362 Liu, L.; Jiang, Y.; Chen, J.; Wang, E.; Bai, X. Tracking Cubic Ice at Molecular
363 Resolution. *Nat.* **2023**, *617* (7959), 86–91.

364 (39) Lee, M.; Lee, S. Y.; Kang, M.-H.; Won, T. K.; Kang, S.; Kim, J.; Park, J.; Ahn, D. J.
365 Observing Growth and Interfacial Dynamics of Nanocrystalline Ice in Thin Amorphous
366 Ice Films. *Nat. Commun.* **2024**, *15* (1), 908.

367 (40) Hong, J.; Tian, Y.; Liang, T.; Liu, X.; Song, Y.; Guan, D.; Yan, Z.; Guo, J.; Tang, B.;
368 Cao, D.; Guo, J.; Chen, J.; Pan, D.; Xu, L. M.; Wang, E. G.; Jiang, Y. Imaging Surface
369 Structure and Premelting of Ice Ih with Atomic Resolution. *Nat.* **2024**, *630* (8016), 375–
370 380.

371 (41) Park, J. S.; Noh, N.; Park, J.; Shim, Y.; Park, S.; Qureshi, Y.; Kang, S.; Huh, Y.; Lee, C.-
372 W.; Yuk, J. M. Phase Transition of Cubic Ice to Hexagonal Ice during Growth and
373 Decomposition. *Nano Lett.* **2024**, *24* (37), 11504–11511.

374 (42) DOWELL, L. G.; RINFRET, A. P. Low-Temperature Forms of Ice as Studied by X-Ray
375 Diffraction. *Nature* **1960**, *188* (4757), 1144–1148.

376 (43) Sargent, D. F.; Calvert, L. D. Crystallographic Data for Some New Type II Clathrate
377 Hydrates. *J. Phys. Chem.* **1966**, *70* (8), 2689–2691.

378 (44) Ghosh, M.; Yang, D.-S. Structures of Self-Assembled n -Alkanethiols on Gold by
379 Reflection High-Energy Electron Diffraction. *Phys. Chem. Chem. Phys.* **2020**, *22* (30),
380 17325–17335.

381 (45) Andersson, O.; Paulo, P. H.; Häussermann, U.; Hsu, Y. J. Evidence Suggesting Kinetic

382 Unfreezing of Water Mobility in Two Distinct Processes in Pressure-Amorphized
383 Clathrate Hydrates. *Phys. Chem. Chem. Phys.* **2022**, *24* (34), 20064–20072.

384 (46) Guo, G.-J.; Zhang, Z. Open Questions on Methane Hydrate Nucleation. *Commun. Chem.*
385 *2021* *41* **2021**, *4* (1), 1–3.

386 (47) Li, L.; Zhong, J.; Yan, Y.; Zhang, J.; Xu, J.; Francisco, J. S.; Zeng, X. C. Unraveling
387 Nucleation Pathway in Methane Clathrate Formation. *Proc. Natl. Acad. Sci. U. S. A.* **2020**,
388 *117* (40), 24701–24708.

389 (48) Jacobson, L. C.; Hujo, W.; Molinero, V. Amorphous Precursors in the Nucleation of
390 Clathrate Hydrates. *J. Am. Chem. Soc.* **2010**, *132* (33), 11806–11811.

391

392 **TOC Graphic**

